small methods
www.small-methods.com

Dissolution Manufacturing Strategy for the Facile Synthesis of Nanoporous Metallic Glass Multifunctional Catalyst

Shenghao Zeng, Wenqing Ruan, Zhe Chen, Shuai Ren, Jihan Jiang, Jiaqing Lin, Heting Zhang, Zhenxuan Zhang, Jianan Fu, Qing Chen, Xiong Liang,* and Jiang Ma**

The quest for heightened energy efficiency is inextricably linked to advancements in energy storage and conversion technologies, wherein multifunctional catalysts play a pivotal role by mitigating the slow kinetics endemic to many catalytic reactions. The intricate synthesis and bespoke design of such catalysts, however, present notable challenges. Addressing this, the present study capitalizes on a novel dissolution manufacturing strategy to engineer self-supporting, nanoporous multifunctional electrocatalysts, circumventing the prevalent issue of customizing catalytic functionalities upon demand. This innovative approach grants the flexibility to finely tune the incorporation of active species and metalloid binders, culminating in the creation of a self-supporting nanoporous metal glass electrocatalyst doped with RuO_2 (NPMG@RuO_2) with outstanding performance in alkaline media. The catalyst showcases superior electrocatalytic activity, achieving low overpotentials of 41.50 mV for the Hydrogen Evolution Reaction and 226.0 mV for Oxygen Evolution Reaction alongside sustained stability over 620 hours.These achievements are attributed to the distinct nanoporous architecture that ensures a high density of catalytic sites and mechanical strength, bolstered by the synergistic interplay between RuO_2 and Pt-based metallic glass. The findings provide a versatile template for the development of nanoporous multifunctional catalysts, signifying a leap forward in the realm of energy conversion technologies.

1. Introduction

Energy is essential for human progress, and renewable sources such as wind, solar, and wave energy are garnering attention for their sustainability and minimal environmental impact.[1] However, issues like geographical limitations and intermittent supply hinder their widespread adoption.[2] As a remedy, advancing energy storage and conversion systems, including fuel cells, water electrolysis devices, and metal–air batteries, is crucial. However, the fundamental electrode reactions that constitute the core of these technologies, primarily the hydrogen evolution reaction (HER), oxygen reduction reaction, and oxygen evolution reaction (OER), are inherently sluggish in nature. Consequently, the requisite of high-performance electrocatalysts becomes indispensable to expedite the reaction kinetics, augment the Faradaic efficiency, and mitigate the Ohmic losses.[3] Complications arise from the simultaneous occurrence of multiple reactions within a single device, which can challenge single function catalysts that are typically optimized for a specific reaction. Introducing separate catalysts for each reaction can lead to cross-contamination and complicate manufacturing processes, impeding overall efficiency and effectiveness.[4] Therefore, the pursuit of versatile multifunctional catalysts, capable of efficiently driving multiple reactions, is a key research direction in the quest for robust and sustainable energy technologies.

The realm of multifunctional electrocatalysts is vibrant and diverse, featuring promising candidates like porous N-doped $NiCo_2O_4$@C[5] and Fe_3C–Co nanoparticles[6] suitable for fuel cells, alongside IrNiTa[7] which has shown potential in water electrolysis applications. In electrode fabrication for electrochemical applications, two main strategies prevail. The first commonly involves a slurry of powdered catalyst, conductive additives, and an insulating binder applied to a conductive substrate.[8] Despite its widespread use, this method is hindered by the necessity of insulating binders. Although it provides structural integrity, it reduces the electrolyte-catalyst contact area, hinders active site accessibility[9] and consequently decreases electrocatalytic

S. Zeng, W. Ruan, Z. Chen, S. Ren, J. Jiang, J. Lin, H. Zhang, Z. Zhang, X. Liang, J. Ma
Shenzhen Key Laboratory of High Performance Nontraditional Manufacturing
College of Mechatronics and Control Engineering
Shenzhen University
Shenzhen 518060, China
E-mail: shuai.ren@szu.edu.cn; xliang@szu.edu.cn; majiang@szu.edu.cn
J. Fu
Department of Mechanics and Aerospace Engineering
Southern University of Science and Technology
Shenzhen, Guangdong 518055, China
Q. Chen
Department of Mechanical and Aerospace Engineering
The Hong Kong University of Science and Technology
Clear Water Bay, Kowloon, Hong Kong 999077, China

The ORCID identification number(s) for the author(s) of this article can be found under https://doi.org/10.1002/smtd.202401109

DOI: 10.1002/smtd.202401109

efficiency while potentially leading to stability issues under high current densities due to catalyst detachment. Alternatively, the second method involves direct electrodeposition of active materials onto conductive substrates such as nickel foam,[10] copper foil,[11] carbon cloth,[12] the fluorine-doped tin oxide coated glasses,[13] and stainless steel.[14] The challenge here lies in controlling the material's microstructure, as overly thick deposits inhibit the substrate from accessing inner active sites, impairing electrode function.[15] Generally, most catalysts in these strategies require additional conductive agents, complicating fabrication and potentially impeding performance due to their inherent non-self-supporting nature. Self-supporting multifunctional catalysts, however, integrate catalytic activity and conductivity, offering a streamlined approach to crafting large-scale electrodes and heralding advancements in electrochemical technologies.[16]

Metallic glass (MG), a novel class of amorphous alloy, is recognized for its exceptionally active surfaces and outstanding corrosion resistance, both of which are crucial for the efficacy of electrocatalysis. The disorder within its atomic structure reveals more active sites during electrochemical reactions, ideal for catalytic processes.[17] Despite its advantages, most MG specialize in single reactions due to their specific compositions.[18] To exploit the full potential of MG, we leveraged its exceptional adhesive properties. In the supercooled liquid region (SLR), MG exhibits a marked decrease in viscosity. With the application of heat or ultrasonic waves, it becomes malleable, assuming a thermoplastic-like behavior.[19] This allows MG to act as a "metal glue," effectively binding different substances and facilitating the molding of desired shapes and forms.[20] The thermoplastic nature of MG further enables the engineering of micro- and nanostructures, which is crucial since the presence of low-coordination sites can dictate catalytic efficiency. These sites can be tuned to adjust reactant binding and favor specific reactions.[21] Consequently, we introduce a novel dissolution manufacturing (DM) strategy or the development of self-supporting, nanoporous multifunctional catalysts (NP Multifunctional Catalysts). This leverages the unique combination of adhesive and catalytic properties inherent to MG, aiming to transcend the current constraints of multifunctional catalyst electrodes. Our approach seeks to harness and amplify MG's distinctive attributes for superior catalytic performance in electrochemical applications.

Our strategy forges NP Mulifunctional Catalysts by fusing MG with active catalytic materials and dissolvable particles, such as NaCl. This process, depicted in Figure S1 (Supporting Information), is tunable; by varying the type and amount of catalytic substance, the catalyst can be customized for targeted reactions. A prime exemplar of this technique's success is the creation of a self-supporting nanoporous MG electrocatalyst doped with RuO_2 (NPMG@RuO_2), which has shown exceptional promise for water electrolysis. Its intricately designed micro-nanocomposite porous structure significantly enhances both activity and stability during theHER and OER in alkaline media. This innovation opens new paths for crafting catalysts with inherent multifunctionality and self-supporting frameworks.

2. Results and Discussion

2.1. Characterization of NPMG@RuO_2 Electrocatalyst

Figure 1a presents the synthesis of the NPMG@RuO_2 electrocatalysts, starting with a Pt-based metallic glass (Pt-MG) alloy composed of $Pt_{57.5}N_{i5.3}Cu_{14.7}P_{22.5}$ (at%). Selected for its excellent flowability,[22] thermal stability, and wide SLR. Pt-MG meets the criteria for thermoplastic formability (Figure S2, Supporting Information).[23] Its viability as a HER electrocatalyst has been established.[24] During synthesis, the Pt-MG alloy is heated to reach its SLR and then pressed to infiltrate the interstices of RuO_2 and NaCl. Subsequent immersion in water dissolves NaCl, creating the NPMG@RuO_2 with a distinct, layered nanoporous architecture. This dissolution process yields NPMG@RuO_2 efficiently and ensures straightforward removal from molds, showcasing the method's convenience and practicality.

Figure 1b shows the surface morphology of the NPMG@RuO_2 via scanning electron microscope (SEM), exposing a network of irregularly sized pores formed following the dissolution of NaCl particles. The larger pore sizes are due to the agglomerated clusters of NaCl particles, whereas, at higher magnification (inset of Figure 1b), the presence of finer pores reflects individual NaCl particle contributions. The cross-sectional SEM image (Figure 1c) demonstrates the porous construct throughout the electrocatalyst's matrix, highlighting the interaction between ruthenium oxide particles and Pt-MG. Complementary energy dispersive spectroscopy (EDS) spectrum analysis (Figure S3, Supporting Information) corroborates that MG functions effectively as a "metal glue" to bond ruthenium oxide within the structure. The X-ray diffraction (XRD) results in Figure 1d reveal both amorphous phases and a distinct RuO_2 peak in NPMG@RuO_2, validating the integration of the MG with ruthenium oxide. The transmission electron microscope (TEM) observations in Figure 1e reveal the material's nanoscale porosity. Particle size distribution analysis, detailed in Figure 1f, indicates an average pore size of 19.43 $\pm$ 4.99 nm. Specific Surface Area with the Brunauer-Emmett-Teller (BET) method measurements (Figure S4, Supporting Information) confirm the hierarchical mesoporous architecture of the NPMG@RuO_2, composed of nano-to-microscale pores. This complexity arises from the interplay between nano-sized and micron-sized salt particles and the spatial domains unoccupied by Pt-MG, elucidating the source of the nanoscale porosity.

To investigate the bonding characteristics within NPMG@RuO_2, TEM was utilized to scrutinize the junction between Pt-MG and RuO_2, as depicted in Figure 1g. This examination unveiled a pronounced interfacial layer, indicating that the bonding extends beyond mere mechanical attachment to include intermolecular forces, wherein the MG acts as a binding medium. The contrast observed in the TEM diffraction patterns highlights the juxtaposition of Pt-MG's amorphous state with the crystalline structure of RuO_2, demonstrating the integration of the two distinct phases. Continued TEM analysis offers a deeper understanding of the RuO_2 crystal lattice. Figure 1h exhibits an enlarged RuO_2 crystal image, while the inverse Fourier transform (IFT) image in Figure 1i verifies the crystalline structure,

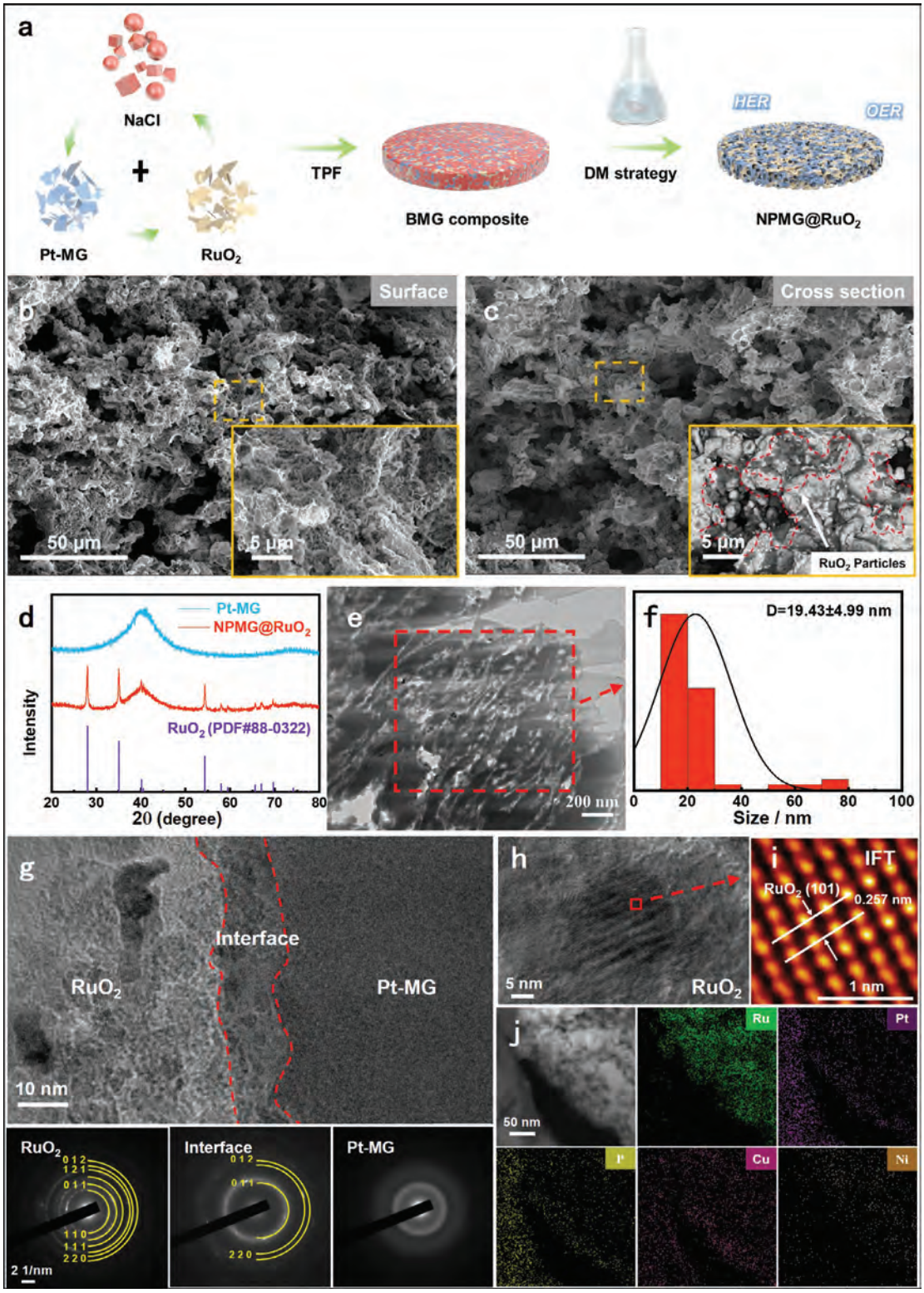

Figure 1. The characterizations of NPMG@RuO_2. a) The schematic diagram for preparation of the NPMG@RuO_2 catalysts using thermoplastic forming (TPF) and DM strategy. b) The SEM images of the micropore on the surface of NPMG@RuO_2. c) The SEM images of micropores in the cross-section of NPMG@RuO_2 and the binding sites of RuO_2 Particles and Pt-MG. d) The XRD patterns of NPMG@RuO_2, Pt-MG and PDF#RuO_2 (PDF#88-0322). e) The TEM images of the nanopores on the NPMG@RuO_2. f) The particle size distribution of NPMG@RuO_2. g) The TEM image of RuO_2 bonded by Pt-MG adhesive. h) The TEM image of the RuO_2 crystal. i) The IFT image of the RuO_2. j) The TEM elemental mapping results of the NPMG@RuO_2.

corroborating the XRD analysis data. These analyses confirm the crystalline integrity of RuO_2 within the composite. The elemental distribution within the NPMG@RuO_2 composite was assessed through TEM imaging and corresponding elemental mapping, as shown in Figure 1j. The mapping highlights the pervasive presence of MG, particularly where MG has infiltrated the irregular surfaces of RuO_2 after softening. This underscores the effective amalgamation of MG within the RuO_2 matrix, providing further evidence of the cohesive structural integration crucial to the performance of the composite.

2.2. Evaluation of Electrocatalytic Performance

To ascertain the electrocatalytic capabilities of the NPMG@RuO_2 samples, a three-electrode configuration was utilized based on the reported work.[25] In this setup, a platinum sheet or graphite rod served as the counter electrode, a Hg/HgO as the reference electrode, and the NPMG@RuO_2 as the working electrode. The assessment was performed in a 1.0 M KOH solution at ambient temperature. In **Figure** 2a, the linear sweep voltammetry (LSV) curves for NPMG@RuO_2, NPMG (nanoporous MG catalyst without RuO_2), the polished MG Plate, and commercial Pt/C (20wt% Pt) are displayed. Current densities were normalized to the geometric area of the electrodes and adjusted for 96% of all resistances. The potential can be converted into reversible hydrogen electrode (RHE) via the following equation (1) (Supporting Information).

Significant variations were observed in the overpotentials needed to attain a current density of 10 mA cm^{-2} among the four materials. The overpotential at 10 mA cm^{-2} (η_{10}) for NPMG@RuO_2 (41.50 mV) was observed to be lower than that for the MG Plate (90.78 mV). This suggests that the incorporation of hierarchical micro- and nano-sized porous structures is beneficial for enhancing catalytic activity. It was found that the hydrophilic and hydrophobic properties of NPMG@RuO_2 contribute to an increased surface area and facilitate the rapid release of H_2 bubbles from the surface. This stands in contrast to the MG Plate electrodes where H_2 bubble adsorption hinders active surface area availability. These phenomena will be discussed in subsequent sections. When tested in alkaline conditions, it was found that the η_{10} for NPMG@RuO_2 (41.50 mV) was more favorable in comparison to that of the commercial Pt/C (58.50 mV). Additionally, the η_{10} for NPMG@RuO_2 was lower than that for NPMG alone (46.50 mV), illustrating the positive effect of RuO_2 on the HER performance.

For an in depth analysis of the catalytic behavior of the catalysts, Tafel plots were generated, and Tafel slopes were determined using the Tafel equation (Equation (2), Supporting Information). In these plots, overpotential η was plotted against log(-j), as seen in Figure 2b. A lower Tafel slope is indicative of more favorable HER kinetics.[26] The NPMG@RuO_2 catalyst was characterized by a Tafel slope of 20.01 mV dec^{-1}, surpassing the benchmark Pt/C catalyst, which exhibited a Tafel slope of 25.85 mV dec^{-1}. Compared to the MG Plate with a slope of 59.34 mV dec^{-1}, the result for NPMG@RuO_2 emphasizes the impact of the nanoporous structure on improving catalytic activity. On the other hand, the Tafel slopes for NPMG@RuO_2 (23.38 mV dec^{-1}) and NPMG (23.38 mV dec^{-1}), which are close to 30 mV dec^{-1}, suggest that the Volmer-Tafel mechanism, with the Tafel step as the rate-determining step (RDS), is applicable. In contrast, the MG plate exhibits a Tafel slope of 59.34 mV dec^{-1}, which is closer to 40 mV dec^{-1}, indicating that the Volmer-Heyrovsky mechanism with Heyrovsky as the RDS is more representative.[25e,27] The Tafel slope for NPMG (23.38 mV dec^{-1}) is also higher than that of the NPMG@RuO_2 catalyst, consistent with the trend observed in the LSV curves, confirming that the addition of RuO_2 to NPMG enhances the HER activity.

The performance of the NPMG@RuO_2 catalyst in OER was evaluated under the same conditions used for the HER assessments. Figure 2c shows the LSV curves (current density normalized to the geometrical area, measured for all resistances compensated for 96%) for NPMG@RuO_2, NPMG, MG Plate, and commercial RuO_2. At the current density of 10 mA cm^{-2}, the overpotential required for NPMG@RuO_2 (η_{10} of 226 mV) was substantially lower than that observed for the polished MG Plate (η_{10} of 447.5 mV) and for the NPMG (η_{10} of 374.5 mV). Furthermore, the performance of NPMG@RuO_2 approached that of the commercial RuO_2 (η_{10} of 213.5 mV), suggesting superior catalytic activity for NPMG@RuO_2 during OER. Additionally, Figure 2d illustrates the derived Tafel slopes obtained for each sample. Notably, the NPMG@RuO_2 exhibited a Tafel slope of 66.53 mV dec^{-1}, which is significantly lower than those of NPMG and MG plate with slopes of 110.42 and 233.61 mV dec^{-1}, respectively. Commercial RuO_2 featured the most minor Tafel slope of 40.72 mV dec^{-1}, indicating its high intrinsic activity. The recorded Tafel slope values highlight the impact of the NPMG@RuO_2 structure in enhancing catalytic OER performance and underscore its potential efficiency in energy applications, approaching that of commercial RuO_2.

For a more comprehensive understanding of the catalytic behavior, electrochemical impedance spectroscopy (EIS) was performed, with the resultant data shown in Figure 2e. An elementary equivalent circuit, comprising a constant phase element, a series resistance (R_S), and a charge transfer resistance (R_{ct}), was applied to model the EIS spectra of NPMG@RuO_2, NPMG, polished MG Plate, commercial Pt/C, and commercial RuO_2. The R_S for the MG Plate, NPMG, and NPMG@RuO_2 were found to be minimal. Notably, the EIS spectrum of the NPMG@RuO_2 catalyst exhibited a semicircular diameter that was significantly reduced in comparison to those of the MG Plate, Pt/C, and RuO_2, indicative of a diminished R_{ct}. A smaller semicircle in the EIS spectrum is reflective of an expedited reaction rate and enhanced charge transportation efficiency. The presence of microscale or nanoscale pores within the catalyst scaffolds is presumed to expose a greater number of active sites in comparison to the MG Plate, thereby lowering the R_{ct}, consistent with the electrochemically active surface area (ECSA) testing result shown in the following discussion. Such a decrease in R_{ct} is advantageous and correlates with an improvement in catalytic performance.

The ECSA of NPMG@RuO_2, MG plate, Pt/C, NPMG, and commercial RuO_2 was deduced from the cyclic voltammetry curves, as presented in Figure S5 (Supporting Information). The variation in current density ($\Delta J/2$), which demonstrated a linear relationship with the scan rate, is illustrated in Figure 2f. This slope corresponds to the double-layer capacitance (C_{dl}), which is directly proportional to the ECSA (Equation (3), Supporting Information). Therefore, comparisons among different

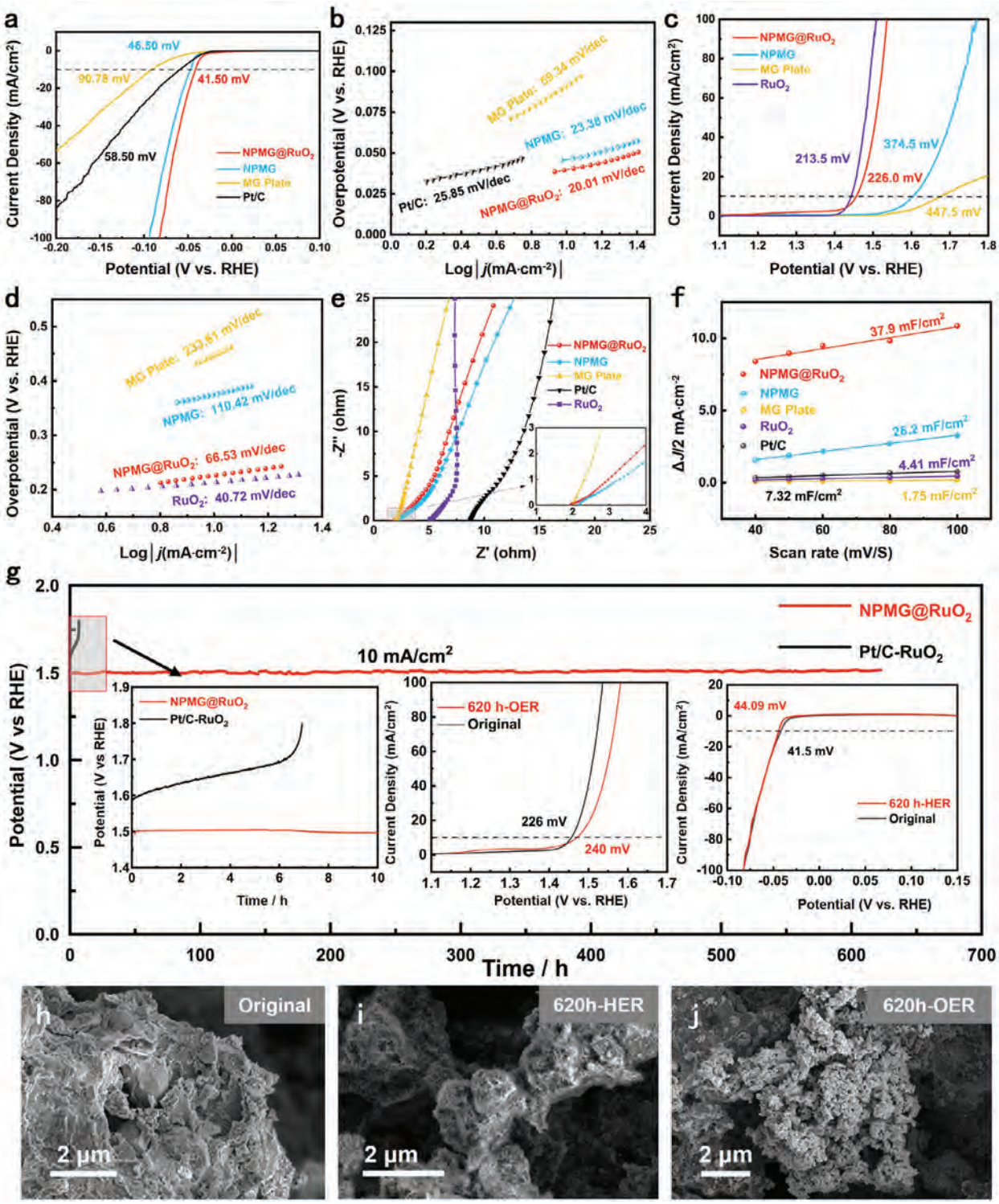

Figure 2. HER and OER electrocatalytic property characterization. a) The HER polarization curves for the NPMG@RuO_2, NPMG, MG Plate, and Pt/C catalysts acquired by LSV with a scan rate of 0.5 mV s^{-1} in 1 M KOH at room temperature. b) Corresponding Tafel slope derived from a) where the Tafel slope is identified. c) The OER polarization curves for the NPMG@RuO_2, NPMG, MG Plate, and RuO_2 catalysts acquired by LSV with a scan rate of 0.5 mV s^{-1} in 1 M KOH at room temperature. d) Corresponding Tafel slope derived from c) where the Tafel slope is identified. e) Nyquist plots of NPMG@RuO_2, NPMG, MG Plate, Pt/C and RuO_2 from 1 000 000 Hz to 0.1 Hz for those samples. f) A linear trend of $\Delta J/2$ as a function of scan rate for those sample. g) Stability tests: chronopotentiometry curves at constant current density of 10 mA cm^{-2}. The illustration is a local enlarged image, and the LSV curves of HER and OER after stability tests. h–j) The SEM images of the surface of the NPMG@RuO_2 for the original sample (Original) without a long-term stability test, the sample after 620 h long-term HER test (620 h-HER), and the sample after 620 h long-term OER test (620 h-OER).

catalysts can be established by evaluating their respective C_{dl} values. For NPMG@RuO_2, the C_{dl} was determined to be 37.9 mF cm^{-2}, a value notably higher than that of the MG plate (1.75 mF cm^{-2}), commercial Pt/C (7.32 mF cm^{-2}), and commercial RuO_2 (4.41 mF cm^{-2}). Such findings indicate that the ECSA of NPMG@RuO_2 is approximately 21 times that of the MG Plate, five times that of Pt/C, and 8 times that of RuO_2. This substantial increase in ECSA points to the effectiveness of the DM strategy, which yields a nanoporous electrocatalyst structure capable of revealing an increased number of active sites conducive to enhanced catalytic activity. Additionally, at a potential of 100 mV versus RHE, the specific activity values (Equation (4) and (5), Supporting Information) clearly demonstrate that NPMG@RuO_2 (0.0206 mA $cm^{-2}{}_{ECSA}$) exhibits over 17% enhancement compared to commercial Pt/C (0.01761 mA $cm^{-2}{}_{ECSA}$), indicating that the individual site activity of our amorphous alloys is significantly higher as shown in the Figure S6 (Supporting Information). The improved performance of our samples benefits from the high activity sites in the amorphous alloys. Durability is a pivotal attribute for electrocatalysts intended for practical applications, alongside the inherent catalytic activity. The chronopotentiometry assay results depicted in Figure 2g reveal that the experiments were performed in an alkaline milieu for 620 h. During this extended assessment, the NPMG@RuO_2 catalyst exhibited a remarkably stable overpotential of 270 mV, demonstrating a resilience that substantially surpasses that of the Pt/C@RuO_2 catalyst. The polarization curve of the overall water electrolysis is shown in Figure S7 (Supporting Information). The polarization curve of the NPMG@RuO_2 with a cell voltage of 1.484 V at a current density of 10 mA cm^{-2}, which is notably lower than that of the commercial Pt/C-RuO_2 (1.503 V). Further performance analyses showed that the NPMG@RuO_2 catalysts sustained their robust catalytic activity for both HER and OER, as evidenced by the durability test extending over 620 h (Figure 2g, inset). Post-test measurements revealed that the η_{10} for HER demonstrated a minimal increase from 41.50 to 44.09 mV. Intriguingly, the Tafel slope for HER displayed a decrease from the pre-test value of 20.01 to 15.63 mV dec^{-1} after the test period (Figure S8, Supporting Information). Pertaining to OER, the η_{10} for the catalyst exhibited a slight elevation from 226 to 240 mV following the 620 h evaluation. Similarly, a marginal increase in the Tafel slope for OER was observed, escalating from 66.53 to 67.56 mV dec^{-1}. An approximate rise of 17 mV in the electrolysis voltage (from 1.498 to 1.514 V) after the 620 h alludes to the potential increase of 2.69 and 14 mV for HER and OER, respectively. This rise in overpotential is inferred to stem from the deactivation of the commercial ruthenium oxide involved in the catalysis process. Thus, employing more stable commercial alternatives, the multifunctional catalyst synthesized via the DM strategy is expected to demonstrate enhanced stability, affirming the wide applicability of this fabrication strategy.

After a prolonged reaction time, the overall porous morphology of the NPMG@RuO_2 catalyst was observed to remain unchanged, as evidenced by the SEM image (Figure S9, Supporting Information) and EDS analysis (Figure S10, Supporting Information). The surfaces of the catalyst for the untreated sample (Original) and after a 620-hour long-term stability test for both HER (620 h-HER) and OER (620 h-OER) are displayed in Figure 2h–j. The images associated with HER after 620 hours reveal a refined needle-like surface morphology, which contributes to an expanded ECSA. This observation resonates with the evolved ECSA measurements (Figure S11, Supporting Information) that display a growth from the original 262.7 to 329.18 mF cm^{-2} after HER stability testing. Additionally, the ECSA after OER testing exhibited a boost to 292.26 mF cm^{-2}. Under OER conditions over the same period, the SEM images show some larger ruthenium oxide particles embellished with increased fine porosity. This morphological change is indicative of the decomposition of some ruthenium oxide particles over the extended reaction time, which modestly elevates the ECSA. Nevertheless, the incremental increase in OER overpotential as the reaction progresses is partly due to the breakdown of ruthenium oxide. Thus, in future research, we plan to explore more stable and efficient OER commercial alternatives,[28] the multifunctional catalyst synthesized via the DM strategy is expected to demonstrate enhanced stability, affirming the wide applicability of this fabrication strategy. Notably, current results position NPMG@RuO_2 as a viable catalytic electrode for commercial water electrolysis applications, maintaining its stability and exhibiting an enlarged ECSA during extended periods of operation.

2.3. Elemental Variations Following Stability Assessments

The nanoporous structure of NPMG@RuO_2 showed remarkable resilience, remaining largely unaltered after extensive stability testing. However, X-ray photoelectron spectroscopy (XPS) analyses disclosed substantive changes in the composition and electronic states on the sample surface after enduring both HER long-term tests (After-HER) and OER long-term tests (After-OER) compared to their pre-tested states (before). As depicted in **Figure 3a**, an increase in the Pt^{2+} peak intensity (After-OER) was noted following the extensive OER, indicative of platinum oxidation relative to the pristine sample (before). Peaks approximately at 74.0 and 79.3 eV were also observed to be more prominent, suggesting additional oxidation to Pt^{4+}. A positive shift (+0.3 eV) was noticed in Pt^0 and Pt^{2+} peaks, suggesting stronger electron binding to the platinum nuclei due to lessened coordination with Ni, Cu, and P.[18a] After long-term HER reactions, no significant valence changes were detected in Pt^0, Pt^{2+} (After-HER), affirming the stability of platinum during HER and its sustained catalytic functionality. Observable oxidation of Ni^0 to Ni^{2+} (After-OER) was evident on the catalyst surface after protracted OER reactions, as shown in Figure 3b, while no distinct changes in Ni were identified after HER. XPS spectra of Cu revealed a decline in the intensity of Cu^0 and Cu^{2+} peaks, suggesting the removal of copper from the surface of NPMG@RuO_2 through selective leaching, evidenced in both OER and HER (Figure 3c). Phosphorus demonstrated a decrease during both HER and OER (Figure 3d), which may point to an increased instability of phosphorus due to inter-atomic coordination on the nanoporous surface as opposed to the interior, facilitating its removal during extended testing.[29] Particularly during HER, the selective leaching of Cu and P was likely to expose more Pt sites on the catalyst surface, which is in agreement with the observed increase in ECSA values for NPMG@RuO_2 (Figure S11, Supporting Information) after the stability test. In the spectral analyses of Ru 3d (Figure 3e) and Ru 3p (Figure 3f), no changes were noted after OER relative

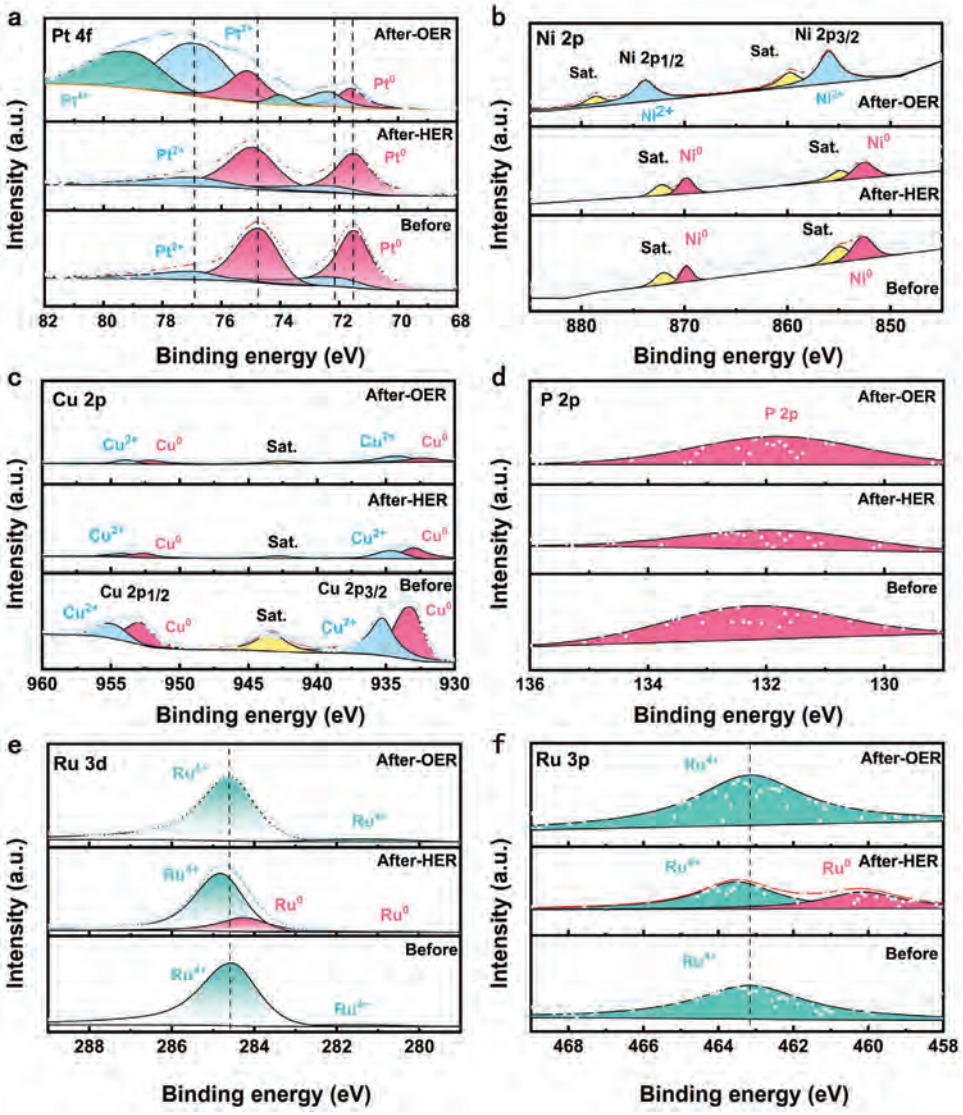

Figure 3. Surface characterization of NPMG@RuO_2: XPS. a) Pt 4f. b) Ni 2p. c) Cu 2p. d) P 2p. e) Ru 3d. f) Ru 3p.

to the sample (Before). However, a partial reduction of Ru^{4+} to Ru^0 was observed following the HER tests.

2.4. Enhancement of HER and OER Performance through Nanoporous Structures

Contact angle assessments were performed on both MG Plate and the innovatively created NPMG@RuO_2 to determine the structural underpinnings of its heightened catalytic performance. As depicted in **Figure** 4a,b, a stark contrast in the water contact angle (WCA) is observed. The nanoporous surface of NPMG@RuO_2 exhibited a minuscule WCA of $3 \pm 1°$, whereas the MG plate, with its unmodified surface, registered a WCA of $62 \pm 2°$ in ambient conditions. This divergence in wettability, attributed to the tailored nanoporosity of the NPMG@RuO_2, aligns with theoretical predictions of the Wenzel model, which posits that micro- and nano-scale surface structures can significantly accentuate wettability through the creation of interstitial sites that retain liquid.[30] The model is mathematically expressed as:

$$\cos \theta^* = r\cos\theta_y \quad (1)$$

where θ^* represents the WCA of the porous MG, r shows the roughness factor, and θ_y is the WCA of a smooth surface. The results clearly affirm that the porous samples fabricated according to the strategy in this paper exhibit exceptionally high hydrophilicity.

Bubble contact angle (BCA) measurements bolster this finding, presenting a BCA of $110 \pm 2°$ on the MG Plate in stark juxtaposition to the $153 \pm 1°$ recorded on the NPMG@RuO_2 surface, an indicator of its superior hydrophobic qualities (Figure 4c,d). Further dynamic wetting analyses reveal that droplets are fully absorbed by the NPMG@RuO_2 surface in under one second, as illustrated in Figure 4e,f, underscoring the material's super hydrophilicity. The BCA on NPMG@RuO_2 demonstrated

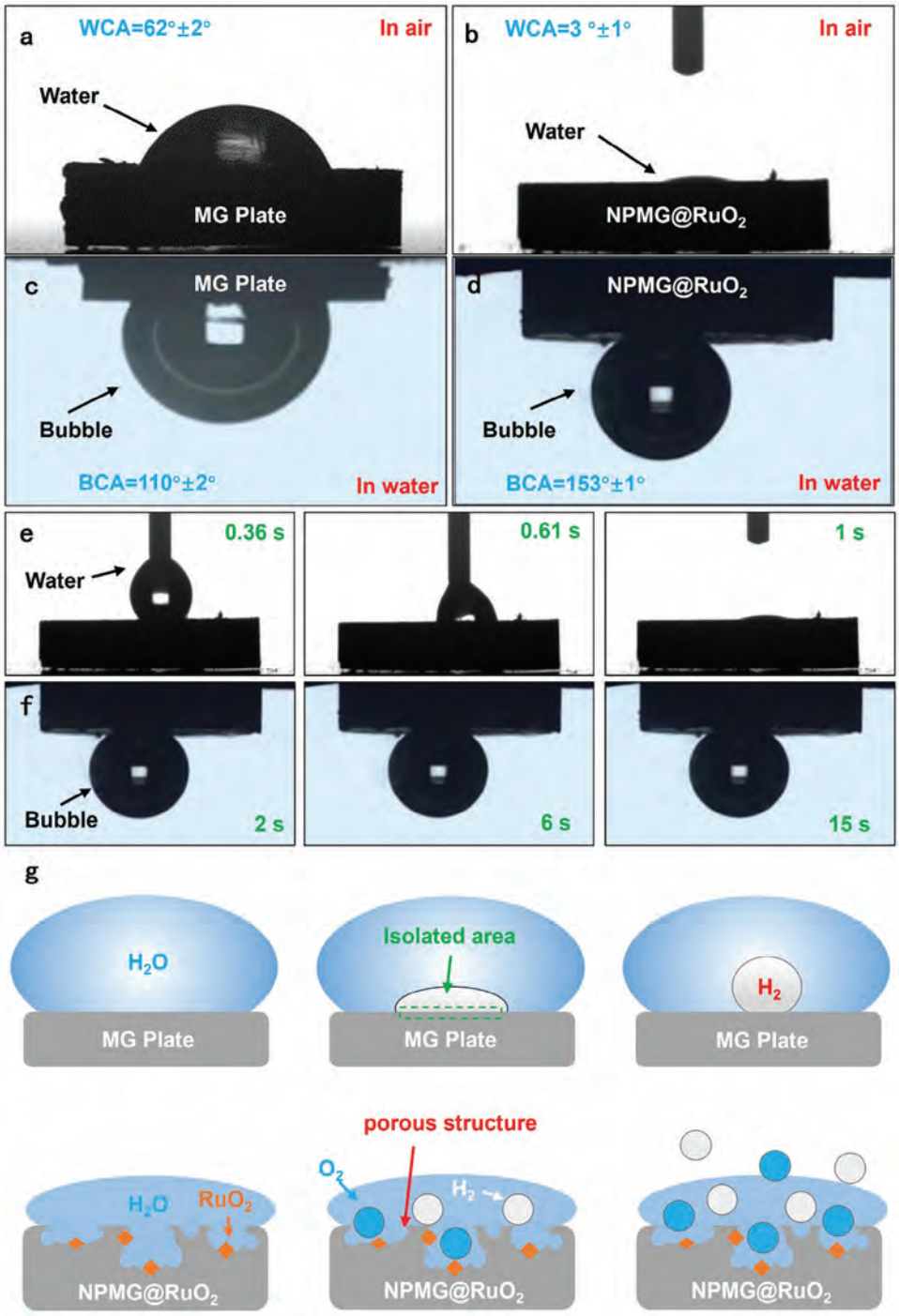

Figure 4. The excellent hydrophilicity and hydrophobicity of the Nanoporous structures. a) The contact angle of the MG plate with a water droplet. b) The contact angle of the NPMG@RuO_2 with a water droplet. c) The contact angle of the MG plate with a bubble. d) The contact angle of NPMG@RuO_2 with a bubble. e) The evolution of a water-drop on NPMG@RuO_2 at the initial stage. f) The evolution of a bubble on NPMG@RuO_2 at the initial stage. g) Sketch of the HER and OER on the surface of the MG plate and NPMG@RuO_2.

remarkable stability, consistently registering at 153 ± 1°. The hydrophilicity and hydrophobicity of the NPMG@RuO_2 surface are crucial in the HER and OER processes.[31] It is demonstrated by Figure 4g that the engineered nanoporous structure of NPMG@RuO_2 provides a significantly enlarged interface with the electrolyte when set against the flat geometry of the MG plate. The increase in the interfacial area is evidenced by more consistent and stronger interactions between water molecules and catalytic sites, which lead to a considerable enhancement in reaction rates, aligning with ECSA and BET method analysis findings. On

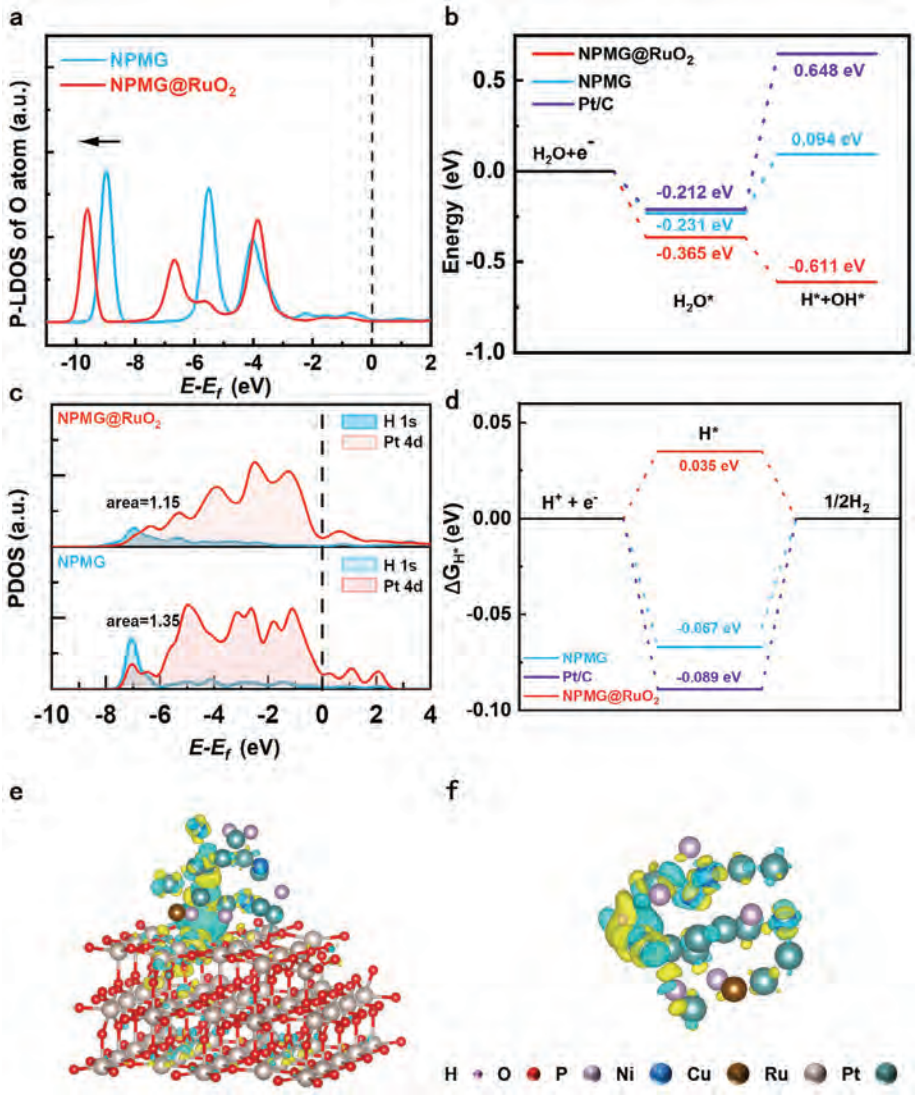

Figure 5. DFT calculations. a) The p-LDOS of oxygen atom in adsorbed water molecule on NPMG@RuO_2 and NPMG. b) The calculated water dissociation barriers on NPMG@RuO_2 and NPMG. The water dissociation barriers of Pt/C are also included for comparison. c) Project density of states for metal 3d orbitals and oxide 2p orbitals with absorbed. d) Free energies of H adsorption on NPMG@RuO_2 and NPMG. The free energy of Pt/C is also included for comparison. Distribution of charge density difference of H adsorbed on the e) NPMG@RuO_2, f) NPMG. The accumulation and reduction of the charge were denoted by yellow and cyan colors, respectively.

the MG plate, it is observed that hydrogen bubbles, produced during catalysis, tend to remain on the surface, leading to the occupation of active sites and a consequent reduction in reaction efficacy. The tailored micro-nanostructure of NPMG@RuO_2, on the other hand, promotes the formation of smaller bubbles and, owing to its hydrophobic nature, facilitates their quick release. This characteristic prevents the blockage of active sites, thereby maintaining continuous accessibility for water molecule interactions.

2.5. Density Functional Theory (DFT) Calculations

To elucidate the intrinsic influence of Ru dopants on the HER activity and to gain insights into electrocatalytic active centers, DFT calculations were conducted. The study incorporated two computational models: NPMG@RuO_2 and NPMG. Compared with the HER mechanism in acidic media, where the hydrogen adsorbate (H*) must be discharged from water in alkaline media, this emphasizes that both the binding strength of hydrogen and the adsorption and activation of water are crucial for overall HER performance.[32] The optimized structure of the intermediate H_2O* and H*+OH* on NPMG@RuO_2 and NPMG, are demonstrated in Figure S12 (Supporting Information).

To further explore the increased water adsorption strength on RuO_2 dopants, according to relevant reports,[33] the p-orbital local density of states (p-LDOS) analysis of the oxygen atom in adsorbed water on NPMG@RuO_2 and NPMG was performed. As indicated in **Figure 5a**, the p-LDOS below the Fermi energy of the oxygen atom in water adsorbed on NPMG@RuO_2 shifts to a lower energy level compared with that on NPMG, suggesting

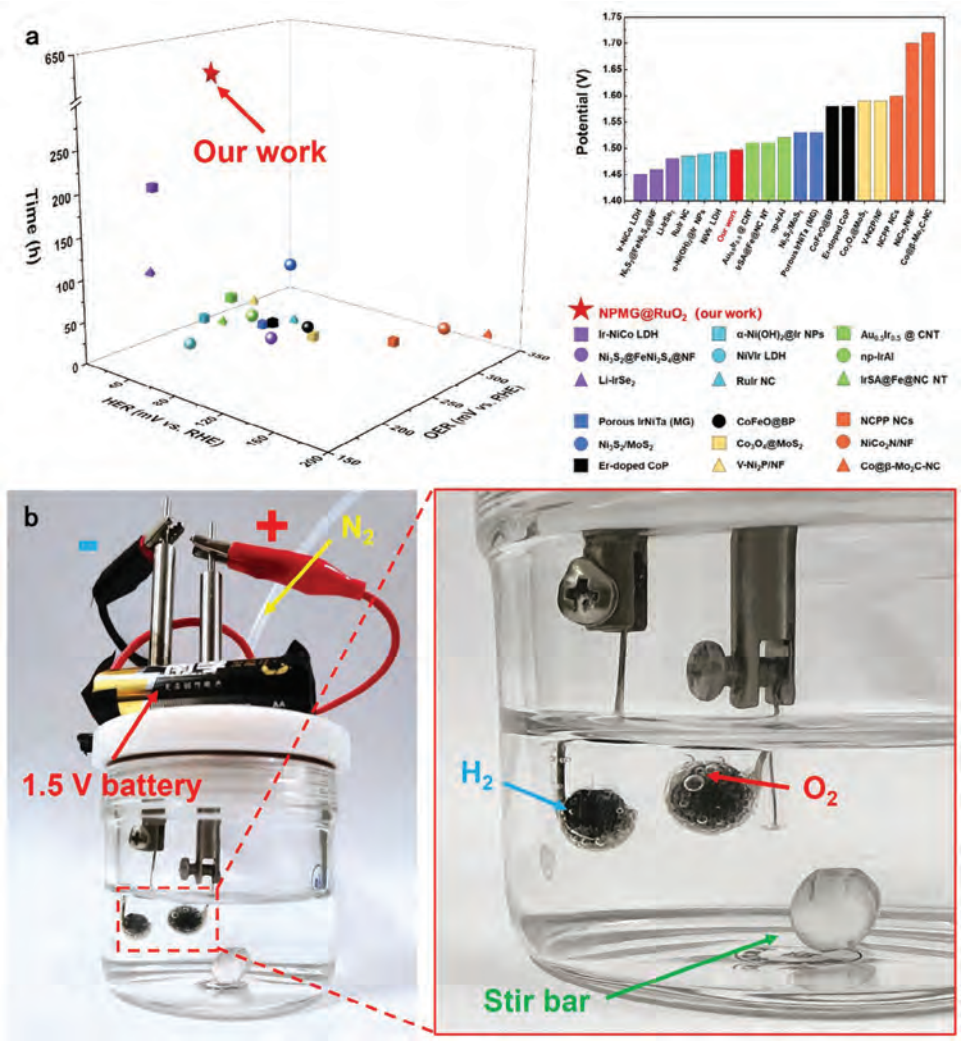

Figure 6. Performance comparison. a) The η_{10}, water splitting voltage, and long-term stability of NPMG@RuO_2 in HER and OER reactions were compared with those reported in the literature for electrocatalysts. More details can be found in Table S1 (Supporting Information). b) The demonstration diagram of 1.5 V battery-driven water splitting.

enhanced stability of water adsorption on NPMG@RuO_2. This increased adsorption strength significantly activates the adsorbed water and lowers the dissociation barrier, as shown in Figure 5b. Therefore, these results suggest that RuO_2 doping could facilitate water dissociation during both the alkaline Volmer and Heyrovsky steps, thereby enhancing alkaline HER activity.

Furthermore, the adsorption free energy of hydrogen (ΔG_{H^*}) serves as a pivotal metric for assessing alkaline HER performance. Prior research has indicated that a lower ΔG_{H^*} can lead to excessively strong hydrogen adsorption, while a higher ΔG_{H^*} may result in too weak adsorption; both scenarios adversely affect the HER rate. Ideally, catalysts exhibiting a ΔG_{H^*} near zero ($\Delta G_{H^*} \approx 0$ eV) are associated with improved HER activity.[34] Figure S13 (Supporting Information) displays the optimized hydrogen adsorption structures on the surfaces of NPMG@RuO_2 and NPMG. The lesser harmonic d-s orbital overlap between Pt 3d and H 1s for NPMG@RuO_2 (1.15) in comparison with Pt 3d in NPMG (1.35), indicates the doping of RuO_2 weakens the interaction between Pt and H atoms in NPMG@RuO_2 (Figure 5c). The free energy diagram for hydrogen on these two surfaces is shown in Figure 5d. The surface of NPMG@RuO_2 demonstrates a lower $|\Delta G_{H^*}|$ of 0.035 eV compared to NPMG (0.067 eV). This reduced energy level signifies a higher HER activity for NPMG@RuO_2, which is consistent with the experimental results presented in Figure 2a. The differential charge pattern further confirms a more substantial charge transfer from H to both Pt and Ru atoms. This redistribution of charges at the interface, compared to regions away from the interface, is clearly depicted in Figure 5e,f.

Therefore, based on the aforementioned results, the enhanced HER activity of the NPMG@RuO_2 catalyst is attributed to the synergistic tuning of water and hydrogen adsorption energies, echoing findings in $M(OH)_2$/Pt systems.[35] The improved H_2O adsorption and optimized H adsorption collectively enhance both the Volmer and Heyrovsky steps in the alkaline HER process.

In the study, *at* η_{10}, the water splitting voltage, and the long-term stability of NPMG@RuO_2 for HER and OER reactions were

compared with those of various electrocatalysts documented in the literature. The comparison encompassed noble metals, transition metal oxides, nitrides, dichalcogenides, phosphides, carbides, borides, and metal-germanides, as presented in **Figure 6**a and Table S1 (Supporting Information). NPMG@RuO_2 was found to exhibit lower overpotentials for both HER and OER in alkaline media and demonstrated exceptional long-term stability. The proficiency of NPMG@RuO_2 was further evidenced by its capability to enable water electrolysis using merely a 1.5 V battery, as illustrated in Figure 6b. This underscores the catalyst's potential for superior performance in electrolytic systems.

3. Conclusions

In this study, a straightforward, adaptable, and customizable method for the synthesis of self-supporting NP Multifunctional Catalysts has been proposed. This technique allows for variations in the incorporation of catalytically active substances as well as the types and ratios of metalloid binders. The NPMG@RuO_2 electrocatalysts, synthesized using the method as mentioned above, exhibit outstanding HER and OER properties in alkaline environments. Overpotentials of just 41.50 mV@10 mA cm^{-2} for HER and 226 mV@10 mA cm^{-2} for OER were achieved. The recorded Tafel slopes for HER and OER are 20.01 and 66.53 mV dec^{-1}, respectively, surpassing the performance of commercial 20% Pt/C and RuO_2 catalysts. EIS tests reveal enhanced reaction kinetics and higher charge transfer efficiency in NPMG@RuO_2. Furthermore, ECSA measurements indicate a significantly larger number of active sites on NPMG@RuO_2—approximately 21-fold greater than MG Plate, fivefold greater than Pt/C, and eightfold greater than RuO_2. It is noteworthy that stability tests have demonstrated the high durability of NPMG@RuO_2, which sustained its performance after 620 h of continuous operation.

The nanoporous structure contributes to an abundance of active sites, accompanied by optimal hydrophilic and hydrophobic properties, vital for its superior electrocatalytic performance and stability in both HER and OER. The synergistic effect arising from the interaction between RuO_2 and Pt-MG also plays a crucial role in elevating the catalyst's efficiency. Thus, the catalyst preparation method presented not only paves the way for the fabrication of robust electrocatalysts but also opens new avenues for the development of multifunctional catalysts.

4. Experimental Section

All experimental details are included in the Supporting Information.

Supporting Information

Supporting Information is available from the Wiley Online Library or from the author.

Acknowledgements

The work was financially supported by the Key Basic and Applied Research Program of Guangdong Province, China (Grant No. 2019B030302010), the NSF of China (Grant Nos. 52371160, 52271150, 52122105, 52201185), the Science and Technology Innovation Commission Shenzhen (Grants No. RCJC20221008092730037 and 20220804091920001) and the National Key Research and Development Program of China (Grant No. 2018YFA0703605). The authors thank the Instrumental Analysis Center of Shenzhen University for the assistance with the Electron Microscope.

Conflict of Interest

The authors declare no conflict of interest.

Author Contributions

S.Z. and W.R. contributed equally to this work. S.Z.: writing—original draft, visualization, methodology, investigation, data curation, conceptualization. W.R.: writing—review & editing, data curation, supervision, and conceptualization. Z.C.: formal analysis, investigation. S.R.: supervision, methodology, resources. J. J.: investigation, conceptualization. J.L.: investigation. H. Z.: data curation, methodology. Z.Z.: supervision, methodology. J.F.: writing—review & editing, methodology, data curation. Q.C.: methodology, formal analysis. X.L.: supervision, resources. J.M.: writing—review & editing, visualization, supervision, resources, conceptualization.

Data Availability Statement

The data that support the findings of this study are available in the Supporting Information of this article.

Keywords

dissolution manufacturing, metallic glass, multifunctional catalysts, nanoporous structure

Received: July 19, 2024
Revised: August 23, 2024
Published online: September 9, 2024

[1] a) P. Poizot, F. Dolhem, *Energy Environ. Sci.* **2011**, *4*, 2003; b) R. J. Detz, J. N. H. Reek, B. C. C. van der Zwaan, *Energy Environ. Sci.* **2018**, *11*, 1653.
[2] a) I. Staffell, S. Pfenninger, *Energy* **2018**, *145*, 65; b) M. Beaudin, H. Zareipour, A. Schellenberglabe, W. Rosehart, *Energy Sustainable Dev.* **2010**, *14*, 302; c) M. Chatenet, B. G. Pollet, D. R. Dekel, F. Dionigi, J. Deseure, P. Millet, R. D. Braatz, M. Z. Bazant, M. Eikerling, I. Staffell, P. Balcombe, Y. Shao-Horn, H. Schäfer, *Chem. Soc. Rev.* **2022**, *51*, 4583.
[3] V. H. Do, P. Prabhu, V. Jose, T. Yoshida, Y. Zhou, H. Miwa, T. Kaneko, T. Uruga, Y. Iwasawa, J. M. Lee, *Adv. Mater.* **2023**, *35*, 2208860.
[4] a) R. O. Sinnott, F. Beuschlein, J. Effendy, G. Eisenhofer, S. Gloeckner, A. Stell, *J. Grid Comput.* **2016**, *14*, 515; b) Y. Li, Y. Sun, Y. Qin, W. Zhang, L. Wang, M. Luo, H. Yang, S. Guo, *Adv. Energy Mater.* **2020**, *10*, 1903120
[5] Y. Ha, L. Shi, X. Yan, Z. Chen, Y. Li, W. Xu, R. Wu, *ACS Appl. Mater. Interfaces* **2019**, *11*, 45546.
[6] C. C. Yang, S. F. Zai, Y. T. Zhou, L. Du, Q. Jiang, *Adv. Funct. Mater.* **2019**, *29*, 1901949.
[7] D. Liu, Z. Song, S. Cheng, Y. Wang, A. Saad, S. Deng, J. Shen, X. Huang, X. Cai, P. Tsiakaras, *Chem. Eng. J.* **2022**, *431*, 134210.
[8] a) N. K. Chaudhari, S. Chaudhari, J. S. Yu, *ChemSusChem* **2014**, *7*, 3102; b) M. Moloudi, A. Noori, M. S. Rahmanifar, Y. Shabangoli, M. F. El-Kady, N. B. Mohamed, R. B. Kaner, M. F. Mousavi, *Adv. Energy Mater.* **2022**, *13*, 2302137.

[9] X. Chen, G. Zeng, T. Gao, Z. Jin, Y. Zhang, H. Yuan, D. Xiao, *Electrochem. Commun.* **2017**, *74*, 42.
[10] F. Duan, Y. Huang, T. Han, B. Jia, X. Zhou, Y. Zhou, Y. Yang, X. Wei, G. Ke, H. He, *Inorg. Chem.* **2023**, *62*, 12119.
[11] D. Li, F. Wang, J. Mao, *Inorg. Chem.* **2023**, *62*, 16283.
[12] P. Ma, N. Lei, B. Yu, Y. Liu, G. Jiang, J. Dai, S. Li, Q. Lu, *Nanomaterials* **2019**, *9*, 1676.
[13] K. Syrek, O. Tynkevych, M. Wojtas, M. Kozieł, Ł. Pięta, L. Zaraska, *J. Ind. Eng. Chem.* **2023**, *126*, 171.
[14] A. F. Alharbi, A. A. M. Abahussain, W. Wazeer, H. El-Deeb, A. B. Ahmed Amine Nassr, *Int. J. Hydrogen Energy* **2023**, *48*, 31172.
[15] N. K. Chaudhari, H. Jin, B. Kim, K. Lee, *Nanoscale* **2017**, *9*, 12231.
[16] N. K. Chaudhari, H. Jin, B. Kim, K. Lee, *Nanoscale* **2017**, *9*, 12231.
[17] a) Y. Liu+, X. L., A. R. Jadhav, T. Yang, Y. Hwang, H. Wang, Y. L. Lingling Wang, A. Kumar, J. Lee, H. T. D. Bui, M. G. Kim, H. Lee, *Angew. Chem.* **2022**, *61*, 202114160; b) J. Masa, P. Weide, D. Peeters, I. Sinev, W. Xia, Z. Sun, C. Somsen, M. Muhler, W. Schuhmann, *Adv. Energy Mater.* **2016**, *6*, 1502313. c) J. S. Kim, I. Park, E. S. Jeong, K. Jin, W. M. Seong, G. Yoon, H. Kim, B. Kim, K. T. Nam, K. Kang, *Adv. Mater.* **2017**, *29*, 1606893; d) G. Chen, Y. Zhu, H. M. Chen, Z. Hu, S. F. Hung, N. Ma, J. Dai, H. J. Lin, C. T. Chen, W. Zhou, Z. Shao, *Adv. Mater.* **2019**, *31*, 1900883; e) C. Schuh, T. Hufnagel, U. Ramamurty, *Acta Mater.* **2007**, *55*, 4067; f) M. Telford, *Mater. Today* **2004**, *7*, 36; g) W. L. Johnson, *MRS Bull.* **2013**, *24*, 42; h) A. Perker, W. L. Johnson, *Appl. Phys. Lett.* **1993**, *63*, 2342; i) Z. P. Lu, C. T. Liu, *Acta Mater.* **2002**, *50*, 3501; j) W. K. Jun, R. H. Willens, P. Duwez, *Nature* **1960**, *187*, 869; k) A. Inoue, *Acta Mater.* **2000**, *48*, 279; l) Y. C. Hu, Y. Z. Wang, R. Su, C. R. Cao, F. Li, C. W. Sun, Y. Yang, P. F. Guan, D. W. Ding, Z. L. Wang, W. H. Wang, *Adv. Mater.* **2016**, *28*, 10293; m) F. Hu, S. Zhu, S. Chen, Y. Li, L. Ma, T. Wu, Y. Zhang, C. Wang, C. Liu, X. Yang, L. Song, X. Yang, Y. Xiong, *Adv. Mater.* **2017**, *29*, 1606570.
[18] a) X. Liang, Z. Liu, J. Fu, H. Zhang, J. Huang, S. Ren, Z. Zhang, Q. Chen, Y. Xiao, W. Ruan, J. Ma, *Nanoscale* **2023**, *15*, 6802; b) Y. Yan, C. Wang, Z. Huang, J. Fu, Z. Lin, X. Zhang, J. Ma, J. Shen, *J. Mater. Chem. A* **2021**, *9*, 5415; c) Y. H. Wang, L. Li, J. Shi, M. Y. Xie, J. Nie, G. F. Huang, B. Li, W. Hu, A. Pan, W. Q. Huang, *Adv. Sci.* **2023**, *10*, 2303321.
[19] a) Z. Chen, S. Ren, R. Zhao, J. Zhu, X. Li, H. Zhang, H. Lin, J. Zhu, S. Sohrabi, W. Ruan, J. Ma, *J. Mater. Sci. Technol.* **2024**, *181*, 231; b) X. Li, L. Li, S. Sohrabi, J. n. Fu, Z. Li, Z. Chen, R. Sun, Y. Zhang, J. Huang, H. Zhang, J. Zhu, X. Chen, K. Song, J. Ma, *Sci. Bull.* **2024**, *69*, 163; c) L. Li, X. Li, Z. Huang, J. Huang, Z. Liu, J. Fu, W. Wen, Y. Zhang, S. Huang, S. Ren, J. Ma, *Nat. Commun.* **2023**, *14*, 6305; d) S. Sohrabi, J. Fu, L. Li, Y. Zhang, X. Li, F. Sun, J. Ma, W. H. Wang, *Prog. Mater. Sci.* **2024**, *144*, 101283.
[20] a) J. Fu, J. Yang, K. Wu, H. Lin, W. Wen, W. Ruan, S. Ren, Z. Zhang, X. Liang, J. Ma, *Mater. Horiz.* **2021**, *8*, 1690; b) J. Huang, X. Yu, L. Li, W. Wang, H. Zhang, Y. Zhang, J. Zhu, J. Ma, *ACS Nano* **2024**, *18*, 2006.
[21] a) S. Chandrasekaran, L. Yao, L. Deng, C. Bowen, Y. Zhang, S. Chen, Z. Lin, F. Peng, P. Zhang, *Chem. Soc. Rev.* **2019**, *48*, 4178; b) S. Nishimura, K. Ebitani, *ChemCatChem* **2016**, *8*, 2303; c) M. A. Ahsan, T. He, K. Eid, A. M. Abdullah, M. F. Sanad, A. Aldalbahi, B. Alvarado-Tenorio, A. Du, A. R. Puente Santiago, J. C. Noveron, *ACS Appl. Mater. Interfaces* **2022**, *14*, 3919; d) S. Chandrasekaran, M. Khandelwal, F. Dayong, L. Sui, J. S. Chung, R. D. K. Misra, P. Yin, E. J. Kim, W. Kim, A. Vanchiappan, Y. Liu, S. H. Hur, H. Zhang, C. Bowen, *Adv. Energy Mater.* **2022**, *12*, 2200409; e) S. Chandrasekaran, E. J. Kim, J. S. Chung, C. R. Bowen, B. Rajagopalan, V. Adamaki, R. D. K. Misra, S. H. Hur, *J. Mater. Chem. A* **2016**, *4*, 13271.
[22] Q. Luo, W. H. Wang, *J. Non-Cryst. Solids* **2009**, *355*, 759.
[23] a) X. Li, X. Liang, Z. Zhang, J. Ma, J. Shen, *Scr. Mater.* **2020**, *185*, 100; b) Z. P. L., C. T. Liu, *Mater. Res. Soc. Symp. Proc.* **2003**, *754*, 26.
[24] T. Nagase, T. Hosokawa, Y. Umakoshi, *Intermetallics* **2010**, *18*, 767.
[25] a) X. Guo, L. Qiu, M. Li, F. Tian, X. Ren, S. Jie, S. Geng, G. Han, Y. Huang, Y. Song, W. Yang, Y. Yu, *Chem. Eng. J.* **2024**, *483*, 149264; b) L. He, M. Li, L. Qiu, S. Geng, Y. Liu, F. Tian, M. Luo, H. Liu, Y. Yu, W. Yang, S. Guo, *Nat. Commun.* **2024**, *15*, 2290; c) L. Li, F. Tian, L. Qiu, F. Wu, W. Yang, Y. Yu, *Catalysts* **2023**, *13*, 1497; d) M. Li, Z. Zhao, W. Zhang, M. Luo, L. Tao, Y. Sun, Z. Xia, Y. Chao, K. Yin, Q. Zhang, L. Gu, W. Yang, Y. Yu, G. Lu, S. Guo, *Adv. Mater.* **2021**, *33*, 2103762; e) X. Guo, M. Li, L. Qiu, F. Tian, L. He, S. Geng, Y. Liu, Y. Song, W. Yang, Y. Yu, *Chem. Eng. J.* **2023**, *453*, 139796.
[26] B. E. Conway, *J. Electroanal. Chem.* **1986**, *198*, 149.
[27] M. Lao, P. Li, Y. Jiang, H. Pan, S. X. Dou, W. Sun, *Nano Energy* **2022**, *98*, 107231.
[28] a) Y. Tan, Z. Zhang, W. Wu, S. Chen, W. Chen, N. Cheng, *Appl. Catal., B* **2023**, *331*, 122684; b) Y. Lai, Z. Zhang, Z. Zhang, Y. Tan, L. Yu, W. Wu, Z. Wang, T. Jiang, S. Gao, N. Cheng, *Chem. Eng. J.* **2022**, *435*, 135102; c) X. Chen, L. Ye, W. Wu, S. Chen, Z. Wang, Y. Zhu, H. Jiang, R. Chen, N. Cheng, *Chem. Eng. J.* **2024**, *487*, 150457; d) R. Chen, Z. Zhang, Z. Wang, W. Wu, S. Du, W. Zhu, H. Lv, N. Cheng, *ACS Catal.* **2022**, *12*, 13234; e) R. Chen, Z. Wang, S. Chen, W. Wu, Y. Zhu, J. Zhong, N. Cheng, *ACS Energy Lett.* **2023**, *8*, 3504.
[29] G. Doubek, R. C. Sekol, J. Li, W. H. Ryu, F. S. Gittleson, S. Nejati, E. Moy, C. Reid, M. Carmo, M. Linardi, P. Bordeenithikasem, E. Kinser, Y. Liu, X. Tong, C. O. Osuji, J. Schroers, S. Mukherjee, A. D. Taylor, *Adv. Mater.* **2015**, *28*, 1940.
[30] R. N. Wenzel, *Ind. Eng. Chem.* **1936**, *28*, 988.
[31] a) X. Zhao, H. Ren, L. Luo, *Langmuir* **2019**, *35*, 5392; b) S. Niu, W. J. Jiang, T. Tang, L. P. Yuan, H. Luo, J. S. Hu, *Adv. Funct. Mater.* **2019**, *29*, 1902180; c) W. Cheng, X. Zhao, H. Su, F. Tang, W. Che, H. Zhang, Q. Liu, *Nat. Energy* **2019**, *4*, 115.
[32] G. C. Yanping Zhu, X. Xu, G. Yang, M. Liu, Z. Shao, *ACS Catal.* **2017**, *7*, 3540.
[33] a) N. Yao, P. Li, Z. Zhou, Y. Zhao, G. Cheng, S. Chen, W. Luo, *Adv. Energy Mater.* **2019**, *9*, 1902449; b) H. Zhang, X. Wu, C. Chen, C. Lv, H. Liu, Y. Lv, J. Guo, J. Li, D. Jia, F. Tong, *Chem. Eng. J.* **2021**, *417*, 128069; c) F. Z. Xing Zhang, S. Zhang, Y. Liang, R. Wang, *Adv. Sci.* **2019**, *6*, 1900090.
[34] a) P. G. M. Berit Hinnemann, J. Bonde, K. P. Jørgensen, J. H. Nielsen, I. C. Sebastian Horch, J. K. Nørskov, *J. Am. Chem. Soc.* **2005**, *127*, 5308; b) J. K. Nørskov, T. Bligaard, A. Logadottir, J. R. Kitchin, J. G. Chen, S. Pandelov, U. Stimming, *J. Electrochem. Soc.* **2005**, *152*, J23; c) W. C. Yoshikazu Ito, T. Fujita, Z. Tang, M. Chen, *Angew. Chem., Int. Ed.* **2014**, *54*, 2131.
[35] a) R. Subbaraman, D. Tripkovic, K.-C. Chang, D. Strmcnik, A. P. Paulikas, P. Hirunsit, M. Chan, J. Greeley, V. Stamenkovic, N. M. Markovic, *Nat. Mater.* **2012**, *11*, 550; b) R. S. N. Danilovic, D. Strmcnik, K.-C. Chang, A. P. Paulikas, V. R. Stamenkovic, N. M. Markovic, *Angew. Chem., Int. Ed.* **2012**, *51*, 12495.